SAND2021-15611C

Instability Measurements in Hypersonic Flow on a Three-Dimensional Cone-Slice-Ramp Geometry

Anshuman Pandey*, Katya M. Casper†, Daniel R. Guildenbecher‡, Steven J. Beresh§, Rajkumar Bhakta ¶, Marie E. DeZetter ‖, Russell Spillers **
Sandia National Laboratories, Albuquerque, NM 87185

This study explores the instability waves occuring at Mach 8 on a slender cone with an axial slice that is followed by either a flat or a 30° spanwise finite ramp. The experiments use high-frequency surface pressure measurements, high-framerate schlieren and a scanning focused laser differential interferometry (FLDI). Comparison with pressure sensors indicates that the dominant second-mode instability waves and the higher harmonics are faithfully captured by the scanning technique. For the expansion only case, the second-mode waves arriving in the upstream cone boundary layer damp out on the slice and lower frequency waves that scale with the new boundary layer thickness grow. Addition of the ramp induces flow separation at the slice corner and upstream second-mode waves propagate along the separated shear layer. In the separation bubble, pressure sensors register a disturbance whose frequency decreases along the separation region. Schlieren visualizations indicate that these are related to the separated shear layer unsteadiness. In addition, coupled separation bubble and separation shock unsteadiness at very low frequency is also observed.

I. Introduction

HYPERSONIC flow around a high-speed vehicle can involve multiple interactions between a thin boundary layer and an expansion, a compression corner, or a combination of both [1]. The evolution of boundary layer instabilities through these geometrical effects play an important role in the transition process that is associated with enhanced heat flux and unsteady pressure loading [1]. Research has historically been focused on canonical two-dimensional expansion or compression only geometries but as pointed out by Dolling [2], there is a need for more flight-realistic geometries to bridge the gap between canonical studies and flight applications. To this end, the present work employs a non-canonical three-dimensional cone-slice-ramp geometry (as shown in Fig. 1) and novel flow measurement techniques towards understanding the interaction between transition-inducing instability waves and a three-dimensional SBLI.

*Postdoctoral Appointee, Engineering Sciences Center, Member AIAA
†Principal Member of the Technical Staff, Engineering Sciences Center, Associate Fellow AIAA
‡Principal Member of the Technical Staff, Engineering Sciences Center, Senior Member AIAA
§Distinguished Member of the Technical Staff, Engineering Sciences Center, Associate Fellow AIAA
¶Test Operations Engineer, Engineering Sciences Center
‖Technologist, Engineering Sciences Center
**Principal Technologist, Engineering Sciences Center

The underlying instabilities of a laminar mean flow can be obtained by linear stability (LST) analysis which governs the temporal or spatial characteristics of the disturbances that would grow by extracting energy from the mean flow. For the high Mach number considered in this work, the Mack second-mode instability dominates the boundary layer characteristics [3–6]. Linear stability analysis and computations at Mach 6 have shown that these instability waves are also present after an expansion corner and no new instability modes were observed [7]. However, the dominant frequency decreases in accordance with an increase in the boundary layer thickness arising from the density decrease after the expansion. Experiments at Mach 6 with a 5° expansion corner have confirmed this behavior where the schlieren results have shown a decrease in the upstream second-mode wave amplitude and an increase in lower frequency waves [8]. Whether this phenomenon also occurs at higher Mach numbers is not known at this time.

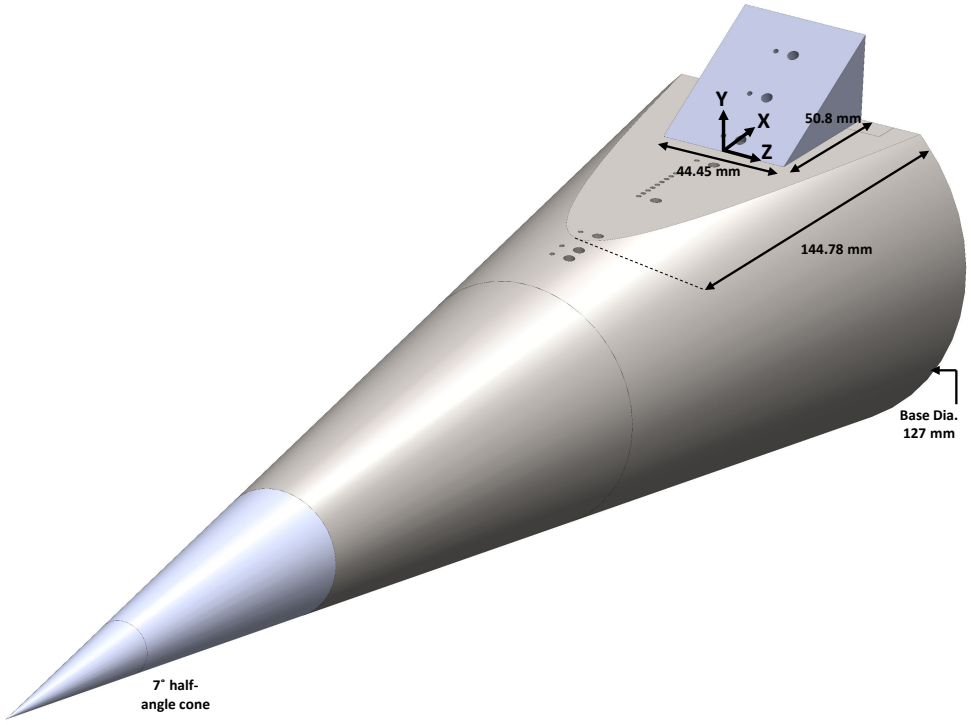

Fig. 1 Schematic of the model used in this work and the coordinate system rooted at mid-span of the slice-ramp corner

The compression corner case is more complicated due to separation of the boundary layer upstream of the corner that generates a separation shock, shear layer, reattachment shock and a separation bubble [9]. Instabilities that are expected to be present in a two-dimensional laminar SBLI are: 1.) upstream boundary layer instabilities, Mack first- and second- modes that manifest as oblique and circumferential waves, respectively, [3–5] 2.) inflection point instability of the separated shear layer that manifests as shear layer flapping and spanwise vortices [10] and 3.) streamwise vortices

near the reattachment region. In terms of interaction of the upstream boundary layer Mack modes with the separated region, linear stability analysis and numerical computations [11–13] have shown that, for a two-dimensional 5.5° degree case at Mach 5.73, the second-mode waves become neutral in the separation bubble and only resume their growth post reattachment. In the separated region, these waves were shown to become a third-mode [11] or a higher order mode depending on the size of the separated region [12]. However, the predominant disturbance magnitude was concentrated along the shear layer [11]. Furthermore, lower frequency first-mode waves were found to be unstable in the separated region [13] where they transformed into second-mode waves [11].

Experimental studies using pressure sensors [14–17] and schlieren visualizations [17] have confirmed that the upstream second-mode waves (third-mode in the separated region according to Balakumar et al. [11]) travel along the separated shear layer and amplify post reattachment on the ramp surface. Inside the separated region, lower frequency peaks have been identified [14, 17, 18] whose origin is not clearly understood. Leinemann et al. [18], who used a 15° compression angle, observed zero lag between two pressure sensors inside the separated region and thus attributed the presence of low frequency pressure peaks to an absolute (non-convective) instability. On the other hand, Butler and Laurence [17] observed a low frequency braided disturbance in the schlieren data and attributed the pressure peak inside the bubble to the convective shear layer disturbances. However, this latter study used a 5° compression angle that resulted in a small separation and allowed placement of only a single pressure sensor inside the bubble. For a large separation case considered in the present work, growth of shear layer instabilities has been found to result in shear layer flapping [19]. However, further work is needed to understand the origin of low frequency peaks inside the separation bubble. Most studies, with the exception of [14, 16, 19], have used two-dimensional geometries, small compression angles and a Mach 6 free-stream. The current study was undertaken at Mach 8 and with a non-canonical geometry.

High-speed boundary layer instabilities on small scale wind tunnel models exist in the 100-300 kHz frequency range with higher harmonics existing up to a few MHz. The need to resolve such high temporal frequencies makes the experiments particularly challenging. Typically, high-frequency piezoelectric pressure sensors such as the PCB132s [20], that can resolve frequencies up to 500 kHz, have been used for characterizing these instability waves. With the advancement of high speed cameras and pulsed laser systems, the bandwidth of a conventional schlieren setup has been improved to be able to capture at least the primary frequency peak of the Mack second-mode [21, 22]. However to characterize the higher frequency harmonics, point-based optical techniques are needed. These include focusing schlieren deflectometry [23] or focused laser differential interferometry (FLDI) [24], that use a high bandwidth (>100 MHz) photodetector. FLDI is based on the aero-optic deflection of a focused beam due to the density and index-of-refraction gradients present in a region of interest. The intereference of a closely spaced pair of beams (a single probe) on a photodetector results in intensity fluctuations whose frequency depends on the frequency of density gradients across the beam path. The focusing aspect of FLDI ensures that the technique is sensitive, at least at high frequencies, to a narrow region near the centerline of a wind tunnel, such that it filters out large scale motions that are

present near the tunnel walls. FLDI has been demonstrated in several hypersonic facilities as being able to measure the boundary layer instabilities [24–28]. Recent works have looked to improve the efficiency of the measurements by extending the single point-based FLDI systems to line-based [27] or multi-point based systems [28] by using appropriate optical elements and photodetection modules to allow these extensions.

In this work, a scanning FLDI system is described with the ability to measure density gradient fluctuations at arbitrary locations in the wind tunnel during a single wind-tunnel run. This scanning system has been demonstrated to capture the instability waves in the separated flow region upstream of the ramp. Furthermore high-frequency pressure measurements and high-framerate schlieren have been used to capture the wide range of frequencies observed in the flow. These measurements provide improved understanding on the evolution of the instability waves that expedite the transition process and the associated increase in heating and pressure loads in compression corner flows. The non-canonical geometry considered in this work is three-dimensional, and has an expansion corner, in addition to the compression ramp, that will help elucidate the difference between such interactions in canonical geometries and flight realistic flows.

II. Experimental Setup

A. Sandia Hypersonic Wind Tunnel and Test Conditions

The Sandia Hypersonic Wind Tunnel (HWT) is a conventional blowdown-to-vacuum facility with an interchangeable system of nozzles and heater sections for the selection of a desired Mach number in the test section. In this work, the Mach 8 system was used that has a 355.6 mm diameter axisymmetric test section. The tunnel employs a bottle farm that stores nitrogen (working fluid) at 689 MPa. A control valve between the high-pressure storage and the tunnel allows a P_0 range of 1720-6890 kPa and an in-line heater provides a T_0 range of 500-890 K. This provides a Reynolds number range from 3.3-20 x 10^6/m with a noise level of $3-5\%$, quantified as the RMS Pitot pressure between 0 to 50 kHz over the mean Pitot pressure. Data presented in this work corresponds to low Re cases from 4.0-6.5 x 10^6/m that result in a laminar inflow in the SBLI region and transition occuring in the shear layer or post-reattachment.

B. Model and Sensors

The test model is a 7° half-angle slender cone with a base diameter of 0.127 m. Fig. 1 shows a schematic of this model and the coordinate system used in this work while a top view is shown in Fig. 2. The cone has an axial cut that creates a slice defined by the hyperbola

$$\frac{(x+466.36)^2}{a^2} - \frac{z^2}{b^2} = 1 \tag{1}$$

where $a = 372.36$ and $b = 46$. The axial length of the horizontal slice is 144.78 mm, and at its aft-end, a spanwise-finite

ramp that is 50.8 mm long and 44.45 mm wide is placed. A flat plate of 0°, i.e. no ramp, provided a baseline case where only the effect of streamwise expansion due to the slice was evaluated. A ramp of 30° angle was used to set up SBLI and the concomitant flow features. The origin is located at the slice-ramp corner and at midspan of the ramp. (x, y, z) coordinates point in the downstream, slice-normal and spanwise directions respectively. This model was mounted using a sting at the base of the cone and all testing was done at zero angle of attack.

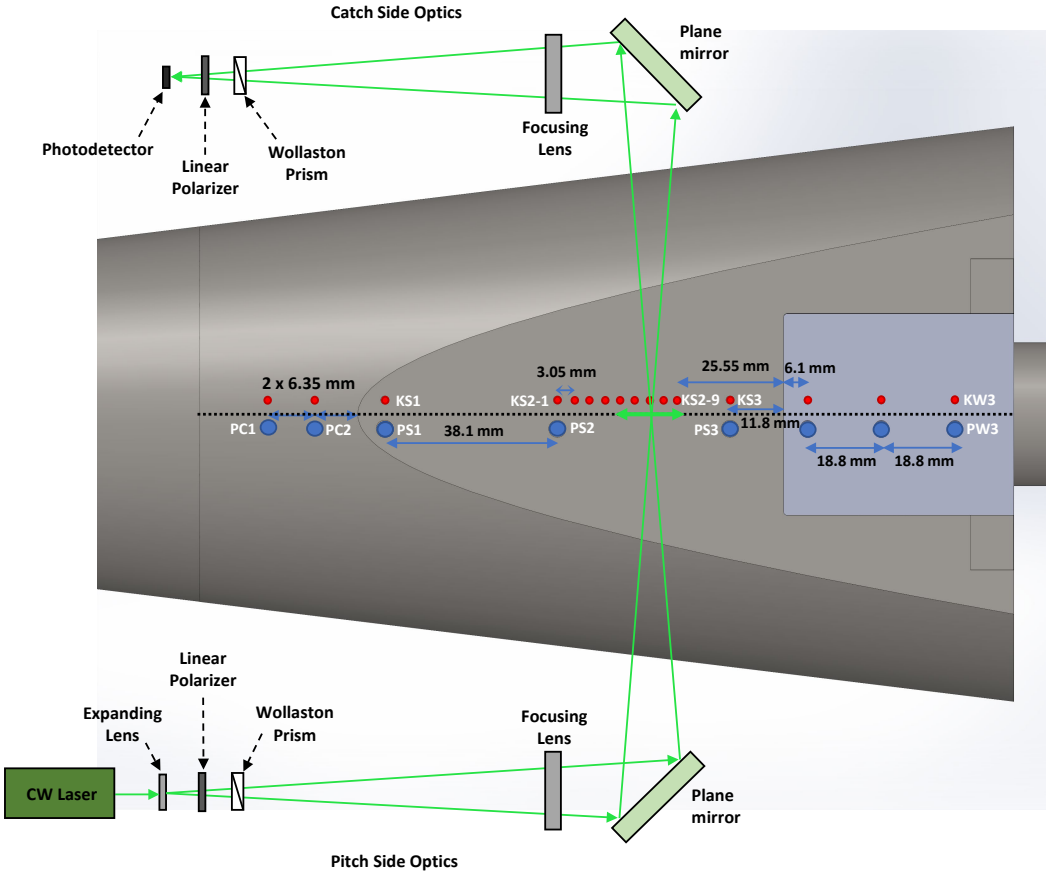

Fig. 2 Schematic showing instrumentation on the model and the FLDI optics. Blue circles represent PCB132 and red circles represent Kulite transducers. Only some sensors are labeled. Distances on the ramp are along the ramp surface. Black dotted line represents the axis of symmetry along which the FLDI probe traverses as shown using green double-headed arrow. Green arrows show the FLDI laser beam path from the pitch side to the catch side. Not to scale.

High-frequency pressure sensors were mounted along the cone, slice and the ramp region in two streamwise rows offset from the centerline by 3.17 mm. One row was mounted with the PCB132s (11-500 kHz) and the other row had Kulite XCQ-30As or XCE-15As (0-50 kHz). These locations are summarized in Table 1 and in Fig. 2. For excitation, the Kulites and the PCB132s used Precision Filters 28144 and PCB 482A22 signal conditioning systems, respectively. Low pass filtering was provided by the Precision Filters system for all the sensors after which the signals were digitized

using a Labview controlled NI PXIe system with NI-6133 and NI-6396 modules. The Kulite signals were low pass filtered at 80 kHz and sampled at 500 kHz. The PCB132s were low pass filtered at 1 MHz; the first three PCBs were sampled at 5 MHz and the rest were sampled at 2.5 MHz.

Table 1 Instrumentation location on the model

Sensor Label	Description	x (mm)	z (mm)
PC1, KC1	1st PCB, Kulite on the cone	-106.6	3.2, -3.2
PC1, KC2	2nd PCB, Kulite on the cone	-100.3	3.2, -3.2
PS1, KS1	1st PCB, Kulite on the slice	-88.0	3.2, -3.2
PS2	2nd PCB on the slice	-49.9	3.2
KS2-1 to KS2-9	2nd through 9th Kulite on the slice (3.1 mm spacing)	-49.9 to -25.5	-3.2
PS3, KS3	3rd PCB and 10th Kulite on the slice	-11.8	3.2, -3.2
PS4, KS4	4th PCB and 11th Kulite on the slice (0° case)	6.1	3.2, -3.2
PS5, KS5	5th PCB and 12th Kulite on the slice (0° case)	24.9	3.2, -3.2
PW1, KW1	1st PCB, Kulite on the ramp (30° case)	5.3	3.2, -3.2
PW2, KW2	2nd PCB, Kulite on the ramp (30° case)	21.6	3.2, -3.2
PW3, KW3	3rd PCB, Kulite on the ramp (30° case)	37.8	3.2, -3.2

C. Scanning FLDI

An FLDI system has two sides, commonly known as the pitch and the catch sides [27], that reside on either side of the measurement volume. An FLDI beam pair is generated on the pitch side and, after passing through the measurement region and getting encoded with the density gradient information, is received on the catch side. In order to make a scanning FLDI system, it is thus important that the pitch and the catch sides move in tandem. This can be achieved by mounting the two sides on individual translation stages; but the precise alignment and synchronization of the two sides can be challenging. Another approach, followed in the present work, is to make the FLDI setup compact by using mirrors to fold the two sides at a right angle and then mounting the whole setup on a single moveable breadboard. If the breadboard itself is mounted on vertical and horizontal translation stages, the FLDI probe can then be placed at arbitrary locations in the measurement volume. For wind-tunnels like the HWT that allow long run times, such a scanning FLDI probe can follow pre-programmed trajectories over the course of a single run, thus improving the efficiency of the measurements. In this work, a horizontal stage has been used that traverses along the wind-tunnel axis as shown in Fig. 3. In future work, this stage may be mounted on a vertical translation stage to allow two-dimensional scans.

A schematic of the FLDI used in this work is shown in Fig. 2. A Coherent Verdi laser set at 50 mW output power was used as the light source, and 532 nm mirrors were used to introduce the beam along the pitch side axis. All optical elements noted in Fig. 2, except the laser, were mounted on a breadboard underneath the HWT as shown in Fig. 3. This breadboard was mounted on a translation stage (Newport IMS500CC) that traversed along the streamwise axis of the wind-tunnel. The pitch side consisted of a 25 mm plano-concave lens (Edmund Optics 47911) that expanded the laser

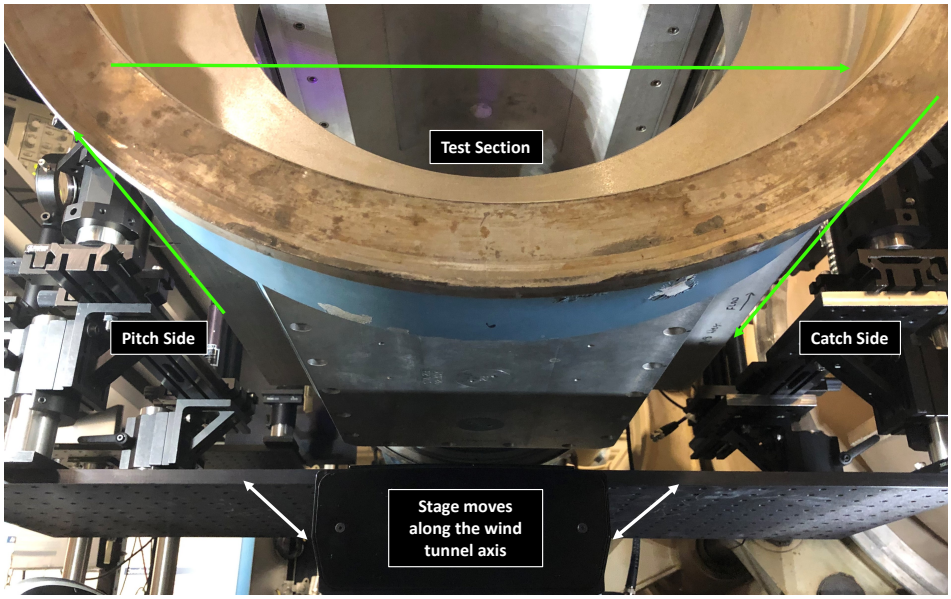

Fig. 3 A photo showing the FLDI setup underneath the HWT test section. Green arrows show the beam path and white arrows show that the stage moves along the wind tunnel axis

beam, a linear polarizer (ThorLabs LPVISA100) and a 2-arcminute Wollaston prism (United Crystals) that split the beam into a diverging beam pair. A 75 mm diameter, 200 mm achromat lens (Edmund Optics 88593) followed by a 101.6 mm 532-nm anti-reflection coated folding mirror focused the beam pair at the centerline of the model (see Fig. 2). A beam profiler (Spiricon LT665) was used to measure the resulting beam diameters that were found to be 0.03 mm with an intra-probe spacing of 0.04 mm.

The catch side optics were symmetrical with a photodetector (ThorLabs PDA10A2) replacing the expanding lens to measure the interference between the beam pair. The photodetector signal was coupled to the data acquisition system using an AC and a DC coupling; the AC signal was typically high pass filtered at 20 kHz to eliminate vibration-induced noise. The two resulting channels were low pass filtered at 2.5 MHz and digitized at 5 MHz. The scanning probe was traversed 152 mm axially at several wall-normal locations along the cone-slice at a speed of 14 mm/s; this speed was determined prior to the runs to traverse the whole slice region during the data acquisition time (limited by the digitizer) of 11.2 s. To change the wall-normal location of the FLDI probe, the optical rails on the pitch and the catch side were each raised by the same amount and the system was realigned. In future work, this step can be eliminated by addition of a vertical stage. Furthermore, the single probe system can be expanded into a scanning multi-probe system by adding appropriate optical elements [27, 28]. The FLDI measurements were made concurrently with the surface pressure measurements.

D. High-Speed Schlieren

Visualization of the instability waves was obtained using a high-framerate schlieren system that incorporated a high-speed laser (Cavilux Smart) and a high-speed camera (Phantom v2512 or Phantom TMX7510). The laser generated pulses of 10 ns duration at high repetition rates - 100/200 kHz for 10 s or 875 kHz for approximately 2000 pulse bursts. The z-type schlieren configuration used two 450.8 mm diameter spherical mirrors for light-collimation and a knife edge oriented horizontally to resolve vertical gradients in density. For the 0° case, a Phantom v2512 at 100 kHz was used with a 640 x 208 pixel area that captured the whole slice-ramp region with a resolution of 2.56 pixels/mm. For the 30° case, a Phantom TMX7510 was used with a 1280 x 288 pixel area that provided a resolution of 7.67 pixels/mm at 200 kHz. This was sufficient to capture the shear layer frequencies. For the Mack second-mode frequencies, a higher frame rate of 875 kHz was selected that limited the active sensor area to 1280 x 64 pixels while preserving the pixel resolution. A thin region covering the separated shear layer was captured by tilting the camera. Since the optical path of the schlieren setup was obstructed by the presence of the FLDI setup, these measurements were made in a separate wind-tunnel entry.

III. Results

The results are divided into two subsections describing the two geometries studied in this work. First, the 0° case is discussed using schlieren and pressure measurements to understand the effect of expansion only on the second-mode waves. Next, the 30° case is discussed with a focus on the various instabilities identified on the geometry. Results from the scanning FLDI are discussed with implications for measuring three-dimensional geometries.

A. Cone-Slice - 0° case

This section presents results on the boundary layer characteristics after the expansion corner for the 0° case. Fig. 4 shows the mean schlieren image, averaged over 0.5s, for the laminar case of Re = 4.2 x 10^6/m. The expansion fan emanating at the corner can be observed in the figure which results in a sharp decrease in density. A rapid growth in boundary layer thickness along the slice can be observed which begins to equilibrate further downstream on the slice. A change in schlieren intesity, due to a decrease in shear outside the boundary layer, can be used to estimate the boundary layer edge at each streamwise location. The wall-normal location where the schlieren intensity values see the strongest drop, quantified as peaks in the second derivative, has been used as the edge location. This estimated boundary layer thickness at each streamwise location is plotted in Fig. 5 along with the estimated curve fits. On a cone, laminar boundary layers exhibit a growth that is proportional to the square root of the distance from the nose [4]. Only a 20 mm segment of the cone is visible in the schlieren field of view where a growth of about 3% is expected. As such, a constant value is fit to the boundary layer edge heights upstream of the slice corner that results in a boundary layer thickness (δ_0) of 2.2 mm. Along the slice, a power law (exponent 0.67) provides the best fit for the streamwise increase in boundary layer thickness. It can be expected that if the boundary layer stays laminar further downstream, the growth

should asymptote to the square root scaling.

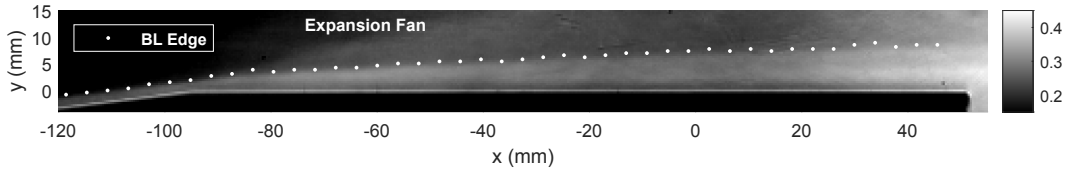

Fig. 4 Mean schlieren image for 0°, Re = 4.2 x 10^6/m. Detected boundary layer edge is marked using white dots

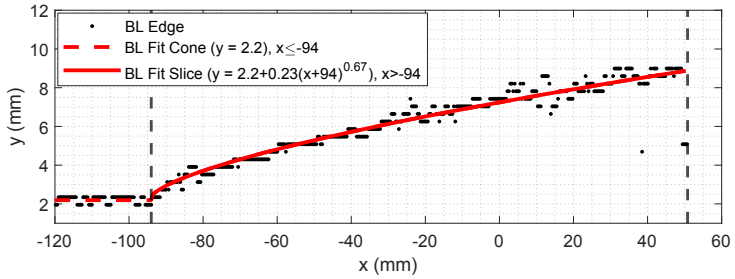

Fig. 5 Boundary layer edge growth along the cone-slice corner. Black dots are the estimated edge heights and red curves are the curve fits.

The effect of expansion on the pressure fluctuations is presented in Fig. 6 through the power spectral density (PSD) of the PCB measurements. This data was taken at Re = 4.6 x 10^6/m and the results are expected to be similar to the Re = 4.2 x 10^6/m case described above. The first two PCBs located on the cone frustum show a dominant 190 kHz peak (f_0) corresponding to the fundamental 2nd Mack mode frequency along with a harmonic at 390 kHz. At PS1, which is located only 6 mm ($< 3\delta_0$) downstream of the corner, a five-fold attenuation in the second-mode peak along with a pronounced down-shift in the harmonic frequency is observed. Fluctuation intensity is lower across all frequency bands indicating strong stabilization of the boundary layer. At PS2 ($20\delta_0$ from corner), the second-mode peak is diminished further by over an order of magnitude (shown using black dashed arrow) and the harmonic is almost non-existent. However, a lower frequency peak around 80-100 kHz is observed. By PS3, a reduction in the upstream second-mode frequency is evident as its magnitude markedly decreases. Further downstream, as the fundamental 2nd mode peak decreases further, the low frequency peak shifts to lower frequencies and increases in amplitude (shown using black solid arrow). Narrow spikes in the spectra at low and high frequencies are attributed to electronic noise.

The most unstable second-mode frequency (f), which corresponds to the frequency of the maximum amplification factor scales as $f = K_1/\sqrt{Re_x}$, where K_1 is a constant [6]. Laminar boundary layer thickness (δ) is related to the stability Reynolds number as $Re_x = K_2(\delta U_e/\nu)^2$. Since the edge velocity (U_e) changes by only about 4% across the expansion, it follows that the product of the most unstable second-mode frequency and the boundary layer thickness should be fairly constant across the cone-slice corner i.e. $f\delta \approx K_3$, where K_3 is a constant. The frequency peaks for the second-mode

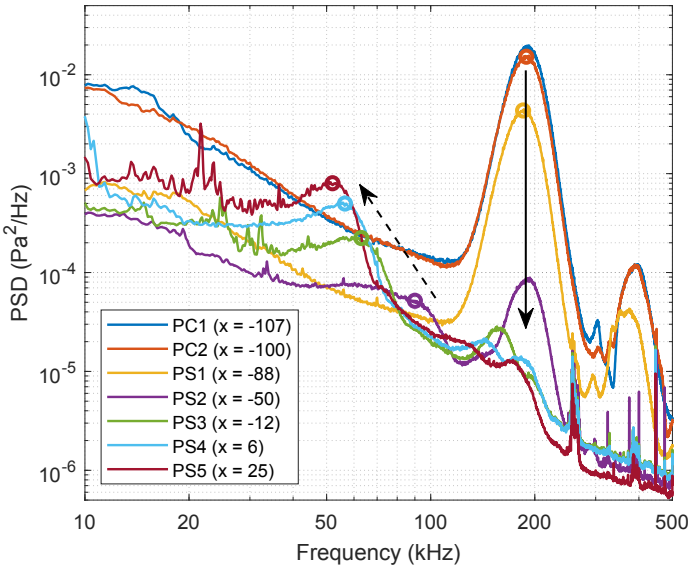

Fig. 6 PSD of PCB sensors for Re = 4.6 x 10^6/m. Black solid and dashed lines indicate drop and growth of upstream and downstream second-mode amplitudes. Circles represent the identified second-mode peaks

waves have been identified from the PSD data and are shown using circles in Fig. 6. For PC2 and PS1, these peaks are identified at the upstream second-mode frequency range (120-250 kHz) whereas for PS3 to PS5, peaks in the lower frequency range (40-120 kHz) were selected. For PS2, the bump around 80-100 kHz was selected assuming that it is due to the amplifying second-mode wave even though its amplitude at that location is less than the decaying upstream wave at 190 kHz. Boundary layer thickness at the corresponding sensor locations have been obtained from the curve fit on the slice in Fig. 5. The product of the identified peak frequencies and the boundary layer thickness is plotted in Fig. 7. It shows a sharp increase just downstream of the corner due to rapid expansion of the boundary layer while the upstream second-mode waves are still present. However, further along the slice the product $f\delta$ realigns to the upstream value. This confirms that the low frequency peaks in the PSD plots in Fig. 6 are due to the growth of the low frequency second-mode waves that become unstable in the expanded boundary layer on the slice. In a recent experimental work at Mach 6 [8] using a 5° cone-cylinder expansion, frequency shifted second-mode waves were observed through spectral analysis of the schlieren visualizations. Furthermore, linear stability analyses with a two dimensional 5° and a 10° corner at Mach 6 have confirmed that no new instability modes are present in the expanded boundary layer except the low frequency second-mode waves [7]. The current results at Mach 8 are in agreement with these studies.

B. Cone-Slice-Ramp - 30° case

In this section, results on the three-dimensional cone-slice-ramp geometry are presented where a 30° spanwise finite ramp has been added to the cone-slice geometry discussed above. First the mean flow features are discussed along with

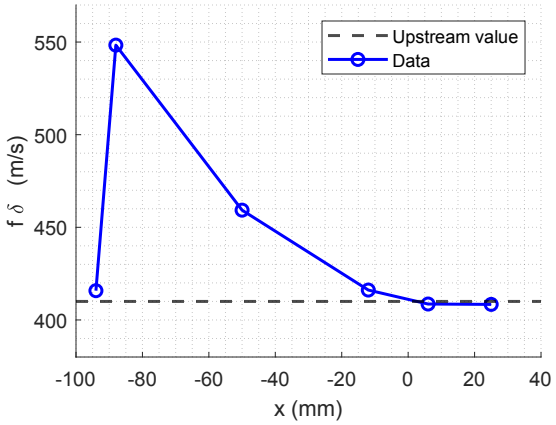

Fig. 7 $f\delta$ variation along the slice

the results from the pressure sensors where key features in the spectra are identified. This is followed by a comparison of the scanning FLDI measurements with the PCB and then schlieren data. In the end, the high frame-rate schlieren data is analyzed.

1. Mean flow organization and pressure fluctuations

The overall flow organization for a laminar case of Re = 4.2 x 10^6/m case is shown in Fig. 8 and Fig. 9 using an averaged schlieren image and an oil flow visualization, respectively. Fig. 8 illustrates the features present in the flowfield such as the shocks arising from the cone nose, separation and reattachment locations. The strong upstream influence in laminar SBLIs is highlighted by the separation of the flow far upstream of the ramp; separated boundary layer develops into a distinct shear layer that impinges slightly downstream of the center of the ramp. Fig. 9 provides a top view of the oil flow visualization that was carried out using a low viscosity fluorescent oil (Zyglo ZL-27A) sprayed on the model prior to the run. This figure highlights the three-dimensionality of this flowfield; the separation location seen at the slice corner in the schlieren image is in fact the vertex of the hyperbolic separation line as visualized by the stagnating oil streaklines. This separation region spills over the horizontal slice emphasizing the far field effect of the ramp on the flowfield.

Pressure fluctuation data is presented in Fig. 10 where only the Kulites colocated with the PCBs are shown. The discussion below is split into separate frequency bands to distinguish the observed phenomena. The upstream cone boundary layer is laminar with no noticeable features in KC2 except the dominant second-mode frequency and its harmonic as seen in the PC2 data. On the slice, PS1 and PS2 spectra show that the surface pressure fluctuations due to the high frequency instability waves decrease dramatically in agreement with the slice only measurements. However, as discussed later, this decrease is primarily due to the propagation of the second-mode waves along the separated shear layer which increases their distance from the surface pressure sensors. As a result, PS3 and KW1 which are in

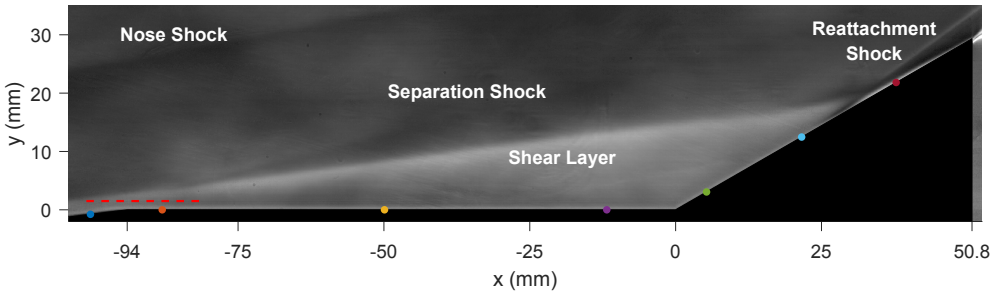

Fig. 8 Mean schlieren image for 30°, Re = 4.2 x 10^6/m. Markers are the sensors locations shown in Fig. 10.

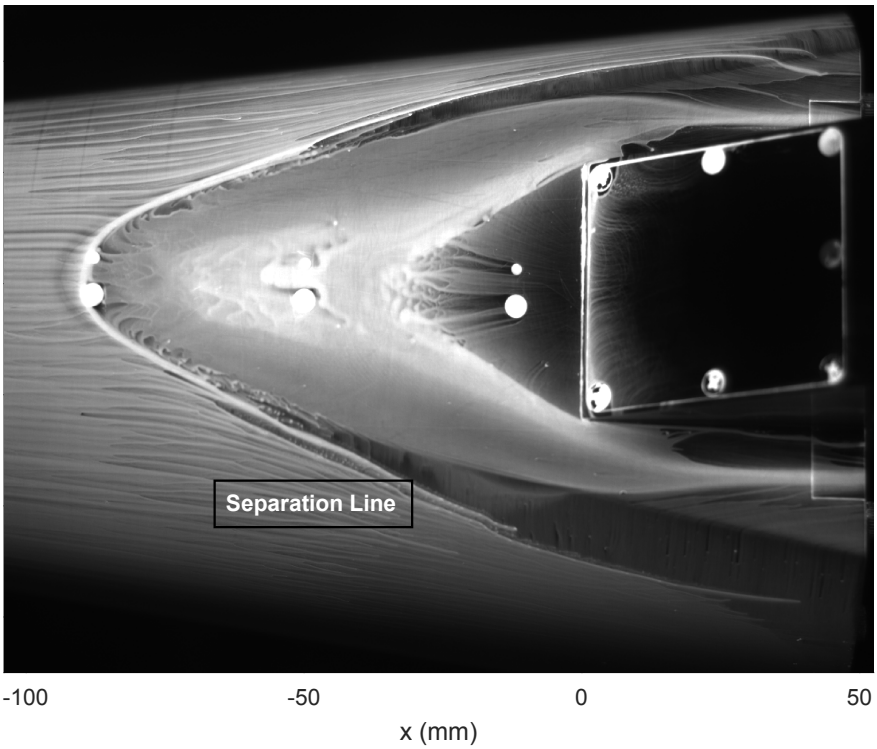

Fig. 9 Oil flow visualization for 30°, Re = 4.2 x 10^6/m.

the deepest part of the separation bubble, register no pressure fluctuations due to the upstream second-mode waves. Close to the reattachment location, PW2 spectra shows that a peak near the upstream second-mode frequency reappears confirming that these waves travelled along the separated shear layer. A slight down shift in dominant frequency of about 20 kHz is also observed. Post reattachment, the dominant frequency does not change as seen in the PW3 spectra. This overall behavior of the second-mode waves in the slice-ramp geometry is in contrast to the slice-only geometry discussed in section III.A where the dominant frequency decreased significantly along the slice.

Downstream of the expansion corner, KS1 and PS1 spectra suggest a broadband decrease in pressure fluctuations except in the ultra-low frequency band of 0-3 kHz. As seen in Fig. 9), this sensor location is very close to the separation

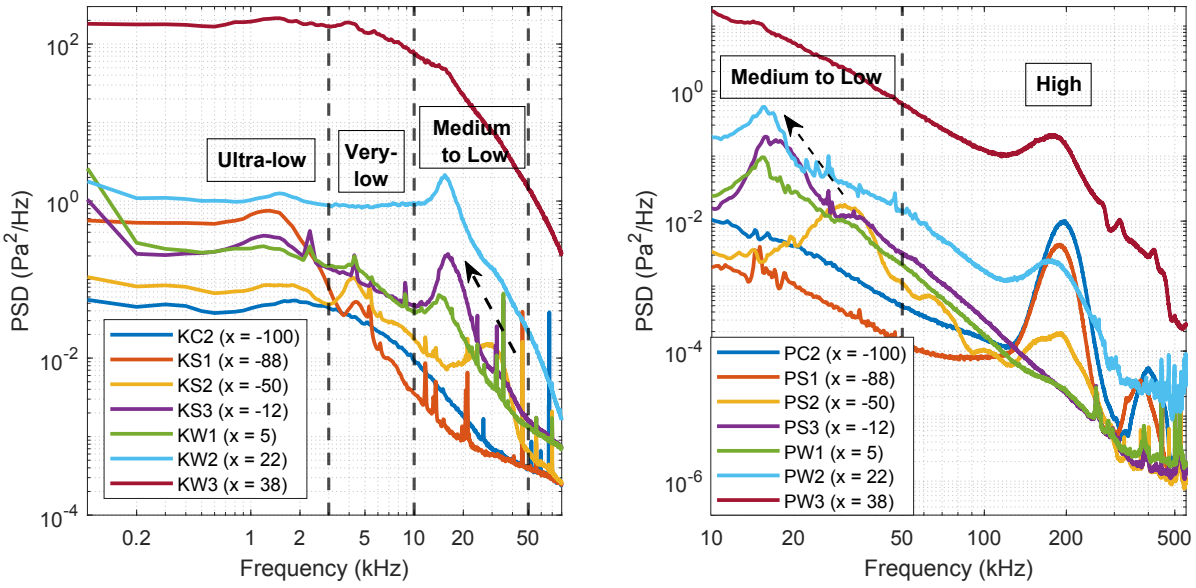

Fig. 10 PSD of surface pressure sensors at Re = 4.2 x 10^6/m. Colors are same as the markers in Fig. 8. (a) Kulite data. (b) PCB data. Dashed lines demarcate the frequency ranges discussed in the text.

line and is well positioned to capture any unsteadiness of the separation shock. Schlieren results, discussed in section III.B.3, confirm that there exists a strong separation bubble breathing unsteadiness in the 0-3 kHz that is associated with separation shock movement. This is in agreement with the separation shock unsteadiness results previously observed at Mach 5 [14]. At Mach 8, the sting used to mount the model (different than the Mach 5 sting) has a structural mode at 1.4 kHz [19] and in a previous study it was unclear if the observed frequency peak in the 0-3 kHz range was due to structural or fluidic effects. However, a recent computational work [29] has confirmed the presence of this unsteadiness indicating that it is related to separation bubble dynamics which could presumably be exaggerated by resonance with the sting structural mode.

The first two sensors on the slice also register a peak in the very-low frequency range of 3-10 kHz, primarily located at 4.4 kHz. This was observed in the schlieren data [19] as a separation shock unsteadiness that couples with shear layer and reattachment shock motion. As discussed in section III.B.3, the higher resolution schlieren (see Fig. 18) obtained in the present work shows second-mode wave packets in the boundary layer upstream of the separation location. This indicates that the arrival of stronger second-mode wave packets has a role to play in this unsteadiness through modulation of the boundary layer characteristics. Naturally occurring wave-packets and the resulting spots can have a preferred frequency that may depend on the receptivity mechanisms including the dominant disturbance environment in the tunnel. At this time, it is hypothesized that an increased intermittency due to the arrival of a large wave-packet can cause unsteadiness of the separation location. However, further correlational work is needed to confirm this hypothesis.

In addition to the above, the KS2 and PS2 sensors located in the middle of the slice also register a medium frequency

peak at 32 kHz and its harmonic at 64 kHz (only in PS2). Further along the slice, the medium frequency peaks shift to the left indicating a low frequency unsteadiness with a primary and a harmonic at 17 and 34 kHz, respectively, for PS3 and 15.5 and 31 kHz, respectively, for PW1. The growth of disturbances inside the separation bubble has been quantified in Fig. 11 using the array of Kulites, KS2-1 to KS2-9. Dominant peaks in the pressure spectra in the 12-45 kHz range have been tracked and a linear decrease in frequency and a simultaneous exponential increase in amplitude of the peaks can be observed. The decrease in frequency arrests by the end of the slice and the peak disturbance stays at a frequency of 15-16 kHz. Simultaneously, the increase in disturbance energy saturates and then, interestingly, decreases from the end of slice to the beginning of the ramp, as seen in both Fig. 10 and Fig. 11. In a previous study using high framerate schlieren, this 16-17 kHz peak was identified as related to shear layer flapping [19]. However, the disturbances in the intermediate band of frequencies observed inside the separation bubble were not tracked. Further discussion on this medium to low frequency unsteadiness is presented in section III.B.3 in the context of schlieren results.

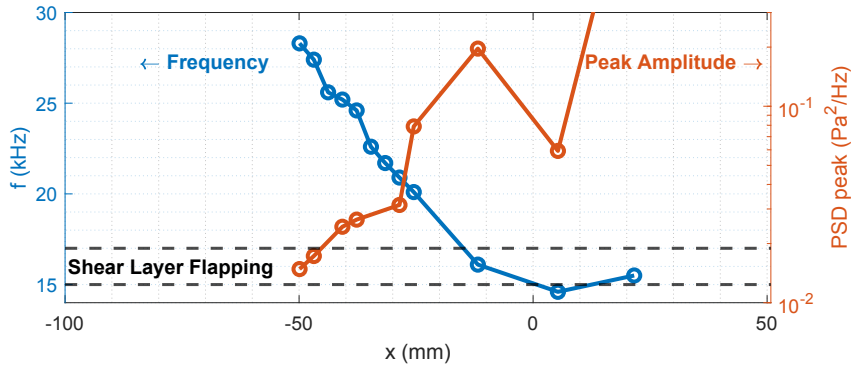

Fig. 11 Amplitude and frequency of peaks in Kulite data (KS2-1 through KW2) in the 12-45 kHz range.

Further downstream, the approach of the impinging shear layer causes a broadband increase in fluctuation magnitudes in both KW2 and PW2 spectra. And after reattachment, the pressure fluctuations (PW3, KW3) are higher across all frequency bands indicating further amplification of broadband disturbances by the reattachment shock. However, a significant peak due to the second-mode waves and small peaks due to medium frequency shear layer flapping and very-low frequency separation-reattachment shock unsteadiness are still visible in the post reattachment spectra.

2. Scanning FLDI measurements

Scanning FLDI was developed in this work to complement the measurements made by surface pressure sensors and high-frame rate schlieren. Since this is the first implementation of a translating FLDI apparatus, this section provides comparisons with other measurement techniques. Previous wind-tunnel studies using FLDI have primarily focused on high-frequency instabilites such as the second-mode waves [24–28] since results at low frequencies are expected to be affected by the flow features near the wind tunnel walls. This is because an FLDI probe becomes exponentially

more sensitive to low frequencies away from the point of focus [30, 31]. Furthermore, unlike the two-dimensional geometries studied in previous works, the three-dimensional curved separation front in the current work (see Fig. 9) can additionally affect the results at low frequencies. In light of the above, the following discussion pertains to the second-mode waves and its harmonics.

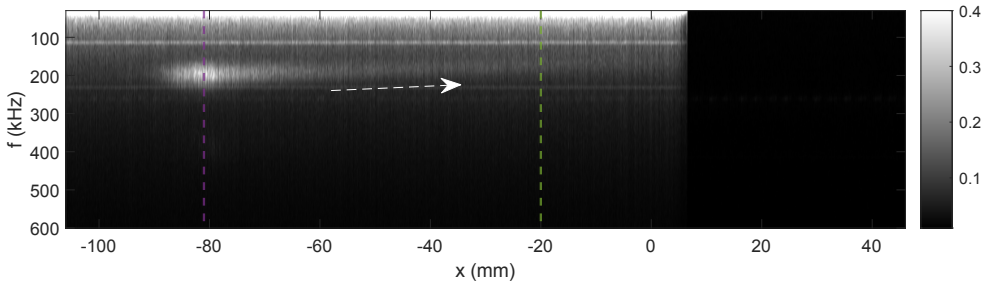

(a)

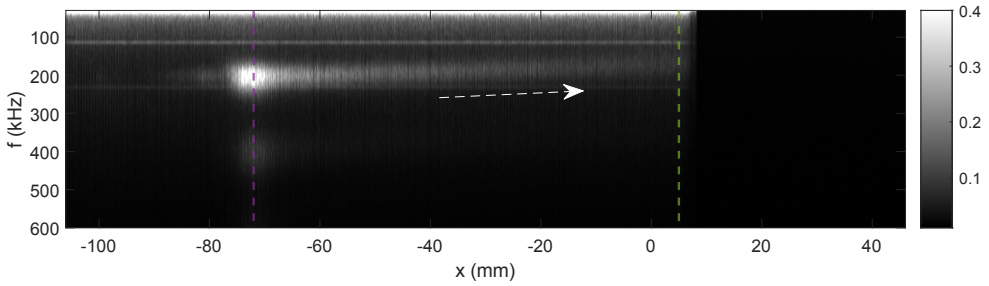

(b)

Fig. 12 Short term fourier transform of FLDI data. (a) Re = 4.2 x 10^6/m, y = 2.5 mm (b) Re = 5.8 x 10^6/m, y = 3.5 mm. Purple and green dashed lines indicate the locations of the signals used for PSD presented in Fig. 13

Fig. 12 shows measurements made at two different conditions of Re = 4.2 x 10^6/m and Re = 5.8 x 10^6/m. The horizontal scans were made along the slice at 14 mm/s starting at 12 mm upstream of the cone-slice corner. Short-term fourier transform (STFT) of the scan signal (raw voltage) was computed to study the frequencies of the density fluctuations observed by the probe during the scan. These STFT contours are shown in Fig. 12. A distinct region of increased fluctutations can be observed, at $x = -81$ and $x = -72$ in (a) and (b), respectively. As discussed below, these increased fluctuation locations correspond to the intersection of the probe path at this wall normal location with the separated shear layer. To compare the dominant frequency in this region, a 2 mm section (which is smaller than the diameter of a PCB132) of the scan signal centered about the probe locations marked in Fig. 13 was analysed. Such a section provided over 700k samples that was sufficient for computing the spectra. Fig. 13 shows that the peak frequency compares well with the second-mode waves present in the cone boundary layer prior to separation. This is in agreement

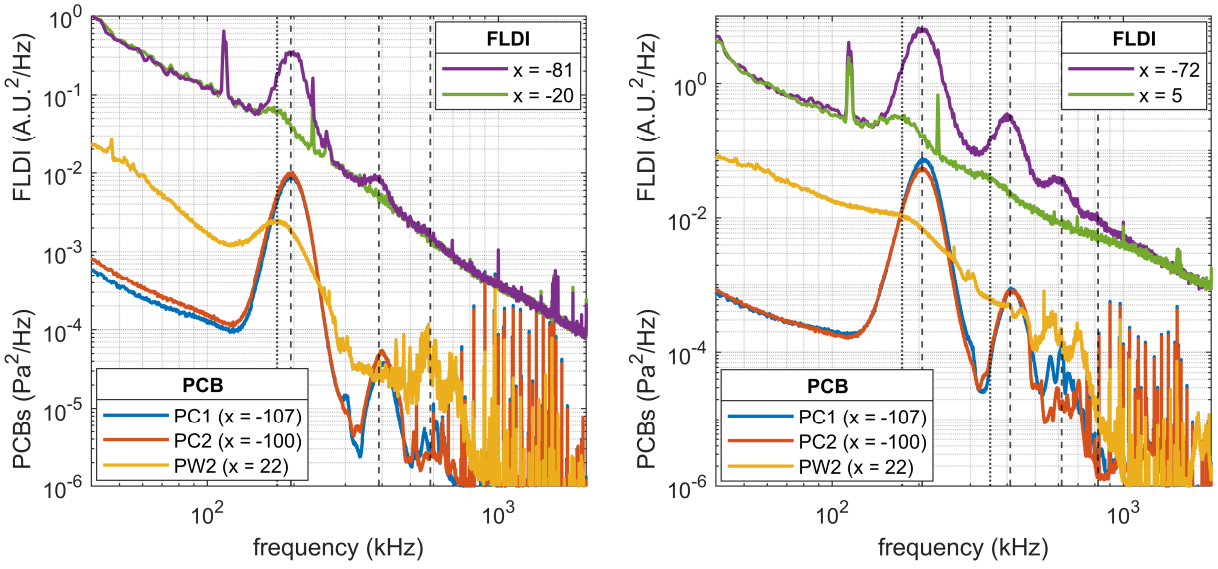

(a) (b)

Fig. 13 Comparison of second-mode frequencies captured by PCB and FLDI. (a) Re = 4.2 x 10^6/m (b) Re = 5.8 x 10^6/m. Locations for FLDI data is marked in Fig. 12

with previous studies [17] that the second-mode waves travel along the separated shear layer and the pressure spectra discussed in previous section. Comparison of second mode amplitudes in PC1 and PC2 spectra suggests that at Re = 4.2 x 10^6/m, the second-mode instability is still growing prior to separation whereas at Re = 5.8 x 10^6/m, it has saturated. This is in agreement with a previous 7° sharp cone transition study in this facility [22]. As such, the amplitudes of second-mode waves are much stronger at Re = 5.8 x 10^6/m and multiple higher harmonics (marked with dashed line) are observed in the FLDI spectra near separation. On the other hand, PCB132s have a frequency limit of about 400-500 kHz and are able to reliably capture only a part of the first harmonic. The STFT contours also show (marked with white dashed arrow) a prolonged tail that shows a gradual shift to lower frequencies. This appears to be due to a gradual decrease in the second-mode frequency along the shear layer (also observed by the high framerate schlieren) whose distance from the probe increases in the downstream direction. A comparison of the frequency from a downstream segment (marked with a green dashed line in Fig. 12) compares favorably with the second-mode spectral peak in PW2 data that is at a frequency 20 kHz lower than the PC2 peak for both the conditions. A noise peak at 115 kHz and its harmonic at 230 kHz is also observed in the PSD plots and the STFT contours as horizontal lines.

Scans at several wall-normal locations were carried out at Re = 5.8 x 10^6/m. STFT contours of these scans in the 130-280 kHz range have been mapped onto a spatial grid of the cone-slice-ramp region where each mm in the wall-normal coordinate is occupied by the STFT contour of the scan at that wall-normal location. The STFT contours have been normalized by the peak amplitude in the 130-280 kHz range and the wall-normal locations where the scans

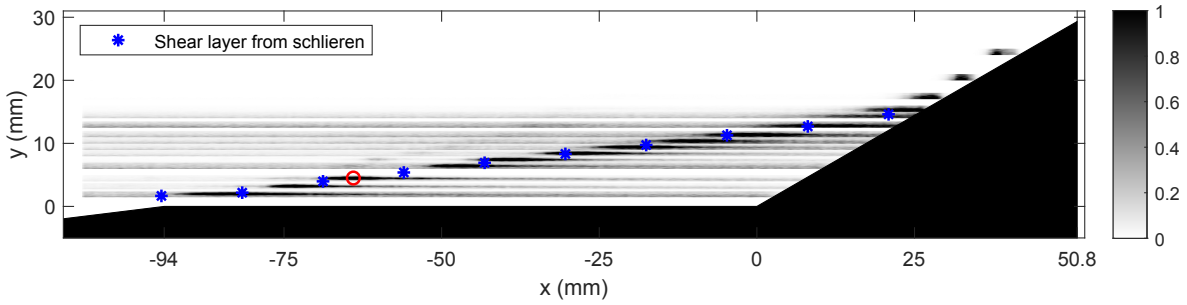

Fig. 14 Disturbance contour obtained in the 130-280 kHz range from FLDI scans. Each horizontal scan shows normalized STFT for a single wall-normal location.

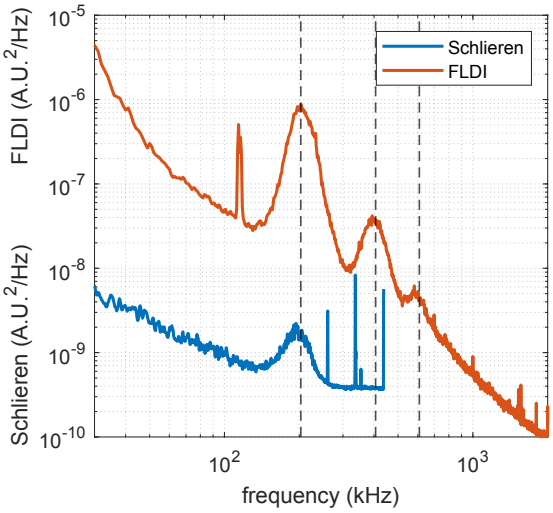

Fig. 15 Comparison of spectra obtained at $x = -64$ mm, $y = 4.5$ mm (red marker in Fig. 14) from high framerate schlieren (Re = 5.5 x 10^6/m) and FLDI (Re = 5.8 x 10^6/m).

were not conducted have been left empty. The resulting contour is presented in Fig. 14 which showcases the power of the scanning FLDI technique. Comparison with schlieren data (blue markers) shows that the spatial distribution of the separated shear layer is well captured and a global picture of the separated flowfield has been obtained by scanning the point probe. In agreement with earlier discussion and previous studies [17], this figure confirms that the second-mode wave energy predominantly travels along the separated shear layer. After reattachment, the disturbance concentrated in the boundary layer become significantly high in comparison to the freestream disturbances thus making the normalized contours appear white above $y = 15$. In comparison to a high-framerate schlieren visualization, such as at 875 kHz employed in this work, the contour in Fig. 14 was obtained at a much higher temporal resolution of 5 MHz and can resolve flowfield frequencies that cannot be studied with schlieren. Fig. 15 shows a comparison of schlieren and FLDI PSD obtained at $x = -64$ mm and $y = 4.5$ mm; this location is shown in Fig. 14 using a red marker. The Re at the two

measurements are slightly different, Re = 5.5 x 10^6/m for schlieren and Re = 5.8 x 10^6/m for FLDI, that results in a 10 kHz difference in the dominant second-mode frequency. More importantly, the superior temporal resolution of FLDI is evident as it is able to capture at least two harmonics (marked with dashed lines) of the dominant second-mode instability. On the other hand, the high-framerate schlieren only captures the dominant second-mode wave and, interestingly, fails to capture even a part of the first harmonic even though it was within the Nyquist limit of the framerate.

3. High-framerate schlieren measurements

This section presents the schlieren measurements carried out in this work starting first with the full view visualizations at 200 kHz. Fig. 16 shows the mode energies obtained by conducting spectral proper orthogonal decomposition (SPOD) analysis [32, 33] on 60 ms of schlieren data with a frequency resolution of 200 Hz. Ample separation between the first two modes indicates meaningful structures are computed as the eigenfunctions of the first SPOD mode [32]. The first mode energy is distributed into several frequency ranges that can be classified as ultra-low (0-3 kHz), very-low (3-10 kHz) and medium to low (10-50 kHz) frequencies. These correspond to the frequency bands identified using pressure spectra in section III.B.1. Discussion below follows the SPOD modes indentified at a few frequencies in each band.

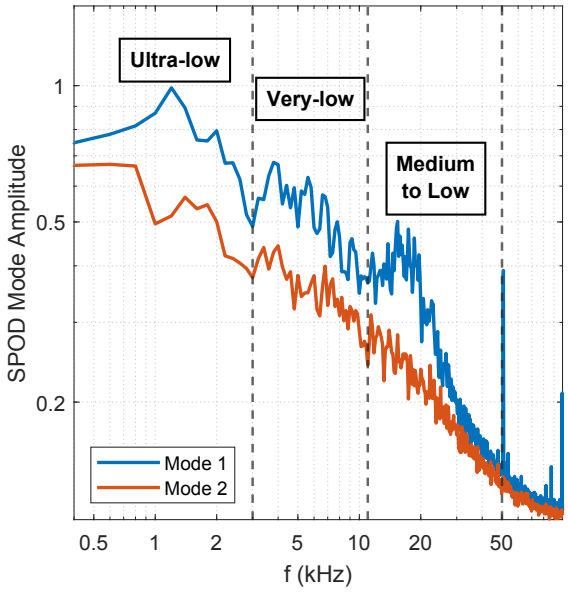

Fig. 16 Schlieren SPOD mode energy

Considering first the ultra-low frequency band, Fig. 17 shows the eigenmode for 1.4 kHz which corresponds well with the peak identified in the KS1 spectra. Since KS1 is close to the mean separation location (see Fig. 8 and Fig. 9), unsteadiness of the separation location is registered by this sensor. Fig. 17 shows a large scale bubble breathing motion that increases (decreases) the size of the bubble and pushes the shock upstream (downstream). The motions of the shear layer and the shock are strongly coupled. As discussed in III.B.1, this is probably exacerbated due to resonance with the sting structural mode that also occurs at 1.4 kHz.

In the very-low frequency band, shown using two frequencies in Fig. 18, a full wavelength of a braiding on the shear layer is visible. This indicates a streamwise undulation of the shear layer that can also be seen to be coupled with the separation shock motion. Close inspection of the cone boundary layer indicates that the arrival of second-mode wave packets has a role to play in this unsteadiness. As discussed in III.B.1, this may be related to a change in the intermittency of the boundary layer that affects its susceptibility to separation; but further work is needed to verify this hypothesis.

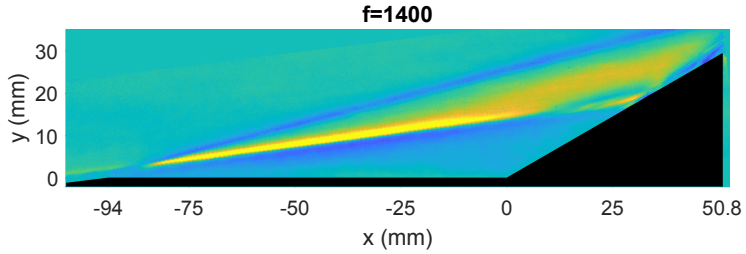

Fig. 17 Schlieren 1st SPOD mode showing ultra-low frequency unsteadiness.

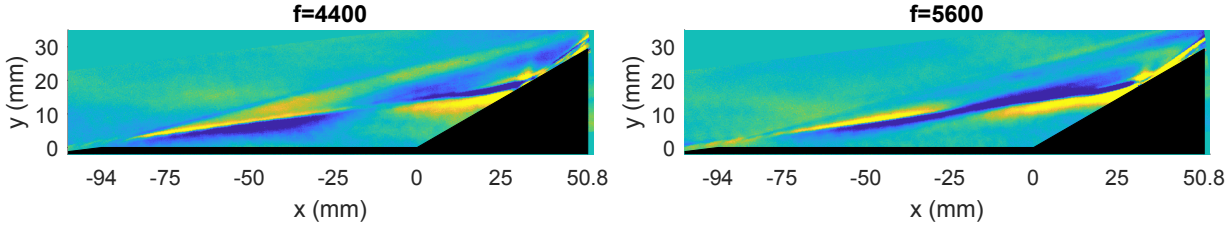

Fig. 18 Schlieren 1st SPOD modes showing very-low frequency unsteadiness.

The low to medium frequency modes are shown in Fig. 19 where considerably less coupling with the separation shock is observed. Increasing frequencies correspond to increasing wavenumbers of braiding in the shear layer suggesting a fairly constant wave speed. Radiation of energy is observed on both sides of the shear layer due to its waviness. On the high speed side (outside) of the shear layer, the freestream is hypersonic and flow deflection in that direction by the shear layer generates shocklets that radiate out into the freestream. On the low speed side (towards the bubble), compression by the shear layer also generates waves that propagate and impinge on the body. Furthermore, the location of the start of the radiation at each frequency appears to be correlated to the location where the waves are the strongest. This happens to be further upstream at higher frequencies, for example, radiation at 17.4 kHz occurs near the slice-ramp corner as compared to 32.6 kHz where it begins mid-way across the slice. This observation indicates that the pressure peaks registered on the slice (see Fig. 11) are indeed related to the unsteadiness of the separated shear layer that radiates pressure and density waves towards the surface.

Another way of visualizing the above is through band-pass filtered PSDs of the schlieren data. The higher framerate

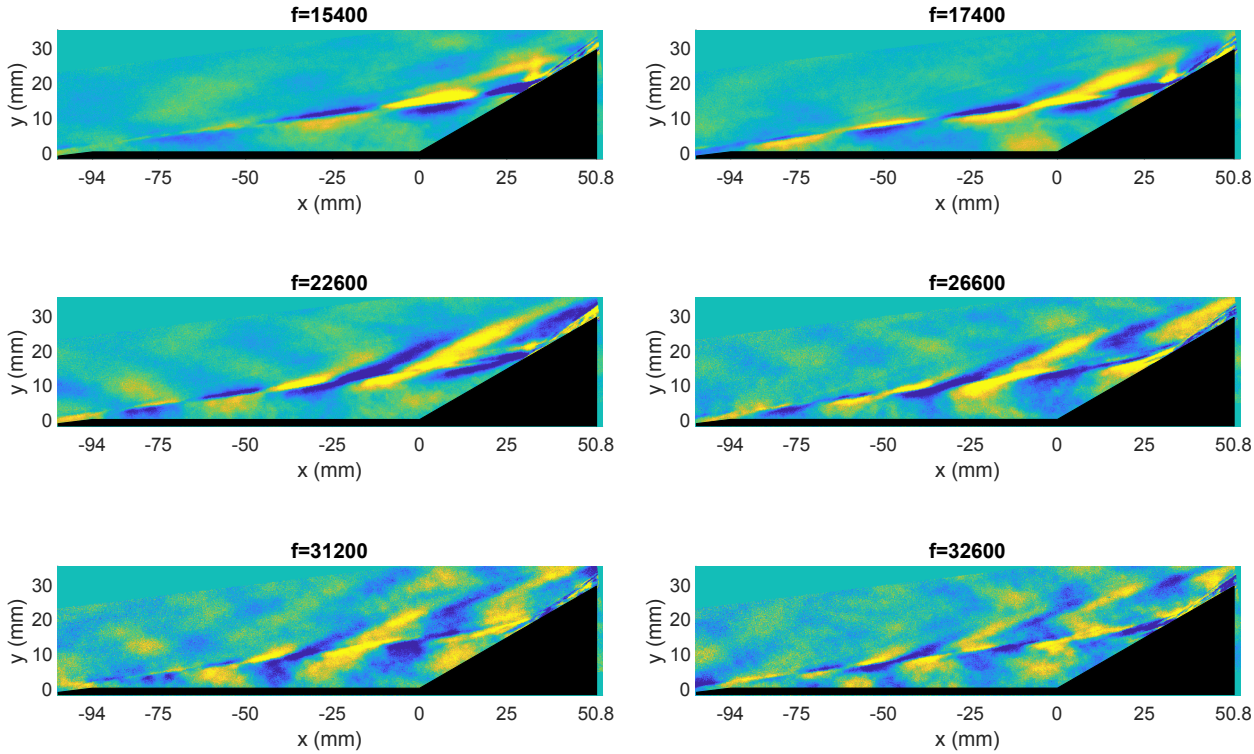

Fig. 19 Schlieren 1st SPOD modes showing medium to low frequency unsteadiness

(875 kHz) schlieren that was acquired in a narrow region bounding the upstream boundary layer and the separated shear layer was used for this purpose. This case corresponds to Re = 4.7 x 10^6/m. Several frequency bands are shown in Fig. 20 with color scale adjusted to showcase the disturbance in the shear layer. Disturbances in all frequency bands are amplified near reattachment indicating the initiation of transition. In agreement with the SPOD results (Fig. 19), the low frequency band of 15-20 kHz has low levels of disturbance until near the end of slice. This is in agreement with the surface pressure measurements (Fig. 11) that show 15-17 kHz peaks near the corner and along the ramp. The location of increased fluctuations shifts upstream as PSDs are averaged at higher frequencies. Development of higher harmonics is also observed such as the 35-40 kHz band shows increased energy near the end of the slice where 15-20 kHz peaks and similarly, 55-60 kHz band shows increased amplitude near $x = -35$ where 25-30 kHz peaks. These results support the observation that not only the primary peaks but also the higher harmonics observed in the slice pressure sensors (for example, 32 and 64 kHz registered by PS2) are due to shear layer disturbances.

Finally, the high frequency second-mode modes are visualized in Fig. 21 using the higher framerate schlieren. In agreement with results from the pressure spectra and FLDI, the second-mode waves arriving in the cone boundary layer are seen to propagate along the separated shear layer. For the Re = 4.7 x 10^6/m, the second-mode waves at the frequency of 184 kHz appear to diminish in strength along the shear layer. This is in agreement with the stability study of Balakumar et al. [11] where the second mode waves (third mode in the separation region) were found to become

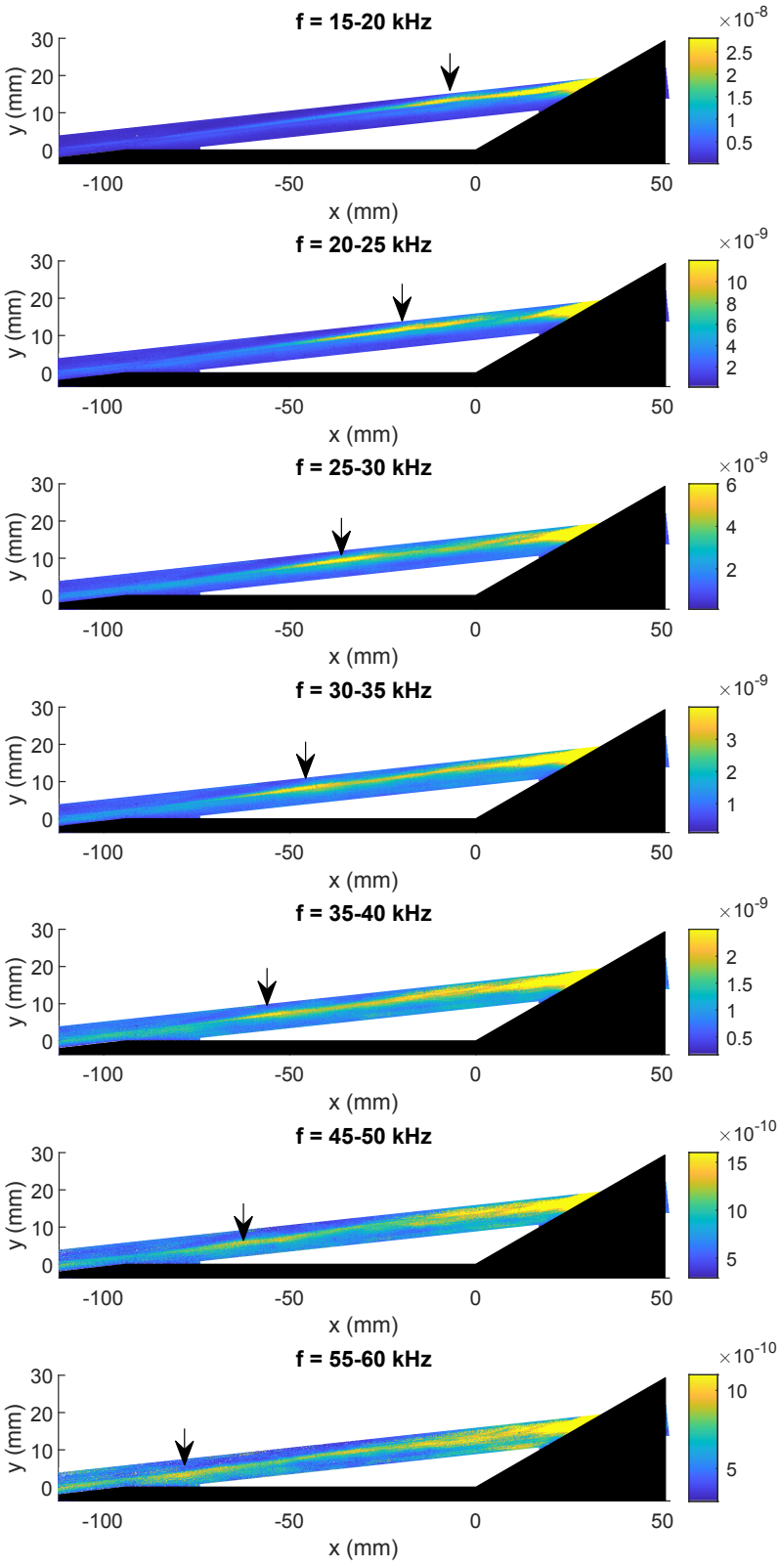

Fig. 20 Schlieren PSD averaged over frequency intervals. Re = 4.7 x 10^6/m

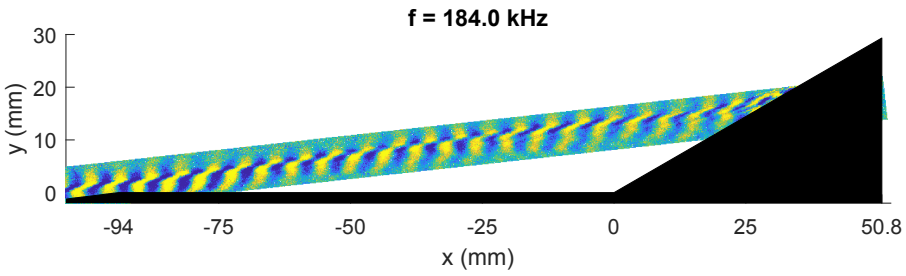

(a)

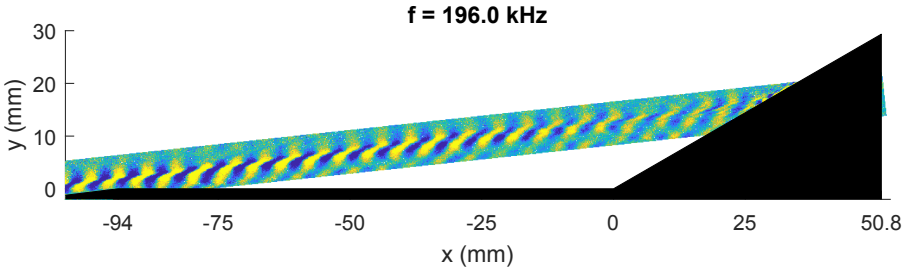

(b)

Fig. 21 Comparison of second-mode frequencies captured by schlieren visualized using 1st SPOD mode. (a) Re = 4.7 x 10^6/m (b) Re = 5.5 x 10^6/m.

neutral. Furthermore, as seen in Fig. 20, the shear layer initiates transition near reattachment which leads to further attenuation of the waves. In contrast, the shear layer in the Re = 5.5 x 10^6/m case is transitional and this results in strong attenuation in second-mode wave disturbance (Fig. 21(b)) near the slice-ramp corner.

IV. Conclusions

Several experimental techniques were used to measure instabilites on a three-dimensional cone-slice-ramp geometry at Mach 8. The following are the primary results:

1. For the expansion-only cone-slice geometry, the second-mode waves present in the cone boundary layer decay rapidly after the expansion corner. After an initial response length, new frequency-shifted waves whose frequency scales with the local boundary layer thickness were identified along the slice.

2. For the cone-slice-ramp geometry, a strong ultra-low frequency (0-3 kHz) breathing motion of the separation bubble was observed that coupled with the separation shock movement.

3. A very-low frequency (3-10 kHz) unsteadiness with coupling between the separation shock motion and long-wavelength shear layer undulation was observed. This could be related to arrival of strong second-mode wave packets that modify upstream boundary layer characteristics and its susceptibility to separation.

4. Medium to low frequency (10-60 kHz) disturbances in the form of streamwise waviness of the shear layer were observed. Starting at about 60 kHz near the separation, the location of peak amplitude shifted downstream with

decreasing frequency until the large-scale shear layer flapping that occurs at 15-17 kHz downstream of the slice-ramp corner. The streamwise waviness causes radiation of shocklets towards the freestream and pressure waves towards the separation bubble. The latter is registered by the surface pressure sensors.

5. Second-mode waves in the cone boundary layer propagate along the separated shear layer while diminishing and shifting to slightly lower frequency.

6. A scanning FLDI technique was implemented that improves the efficiency of single-point FLDI measurements for long duration tunnels like the HWT. It was demonstrated that it can successfully capture second-mode waves and multiple harmonics in the shear layer.

Further examination of the data set using coherence analysis between pressure sensors, FLDI and schlieren is currently underway to understand the various unsteady mechanisms documented in this work. In addition, measurements at higher Reynolds numbers covering transitional and turbulent boundary layers are also being studied. These results will be presented at a future conference.

V. Acknowledgments

Thomas Grasser designed the wind-tunnel model and Daniel Richardson provided the translation stage and valuable suggestions during experimentation. This work was partially supported by the Laboratory Directed Research and Development program at Sandia National Laboratories. Sandia National Laboratories is a multi-mission laboratory managed and operated by National Technology and Engineering Solutions of Sandia, LLC., a wholly owned subsidiary of Honeywell International, Inc., for the U.S. Department of Energy's National Nuclear Security Administration under contract DE-NA0003525.

References

[1] Anderson, J. D., *Hypersonic and high-temperature gas dynamics*, 3rd ed., American Institute of Aeronautics and Astronautics Inc, AIAA, 2019. doi:10.2514/4.105142.

[2] Dolling, D. S., "Fifty years of shock-wave/boundary-layer interaction research: What next?" *AIAA Journal*, Vol. 39, No. 8, 2001, pp. 1517–1531. doi:10.2514/2.1476.

[3] Mack, L. M., "Linear Stability Theory and the Problem of Supersonic Boundary-Layer Transition," *AIAA Journal*, Vol. 13, No. 3, 1975, pp. 278–289. doi:10.2514/3.49693.

[4] Stetson, K. F., Thompson, E. R., Donaldson, J. C., and Siler, L. G., "Laminar Boundary Layer Stability Experiments on a Cone at Mach 8. Part 1: Sharp Cone," *AIAA 16th Fluid and Plasma Dynamics Conference*, AIAA, Danvers, MA, 1983. doi:10.2514/6.1983-1761.

[5] Fedorov, A., and Tumin, A., "High-Speed Boundary-Layer Instability: Old Terminology and a New Framework," *AIAA Journal*, Vol. 49, No. 8, 2011, pp. 1647–1657. doi:10.2514/1.J050865.

[6] Marineau, E. C., Grossir, G., Wagner, A., Leinemann, M., Radespiel, R., Tanno, H., Chynoweth, B. C., Schneider, S. P., Wagnild, R. M., and Casper, K. M., "Analysis of Second-Mode Amplitudes on Sharp Cones in Hypersonic Wind Tunnels," *Journal of Spacecraft and Rockets*, Vol. 56, No. 2, 2019, pp. 307–318. doi:10.2514/1.A34286.

[7] Chuvakhov, P. V., Egorov, I. V., Ilyukhin, I. M., Obraz, A. O., and Fedorov, A. V., "Boundary-Layer Instabilities in Supersonic Expansion Corner Flows," *AIAA Journal*, Vol. 59, No. 9, 2021, pp. 3398–3405. doi:10.2514/1.J060145.

[8] Butler, C. S., and Laurence, S. J., "Interaction of second-mode wave packets with an axisymmetric expansion corner," *Experiments in Fluids*, Vol. 62, 2021, p. 140. doi:10.1007/s00348-021-03235-2.

[9] Arnal, D., and Délery, J., "Laminar-turbulent transition and shock wave/boundary layer interaction," *RTO AVT Lecture Series on "Critical Technologies for Hypersonic Vehicle Development" RTO-EN-AVT-116*, 2004.

[10] Martens, S., Kinzie, K. W., and McLaughlin, D. K., "Measurements of Kelvin-Helmholtz Instabilities in a Supersonic Shear Layer," *AIAA Journal*, Vol. 32, No. 8, 1994, pp. 1633–1639. doi:10.2514/3.12153.

[11] Balakumar, P., Zhao, H., and Atkins, H., "Stability of Hypersonic Boundary Layers over a Compression Corner," *AIAA Journal*, Vol. 43, No. 4, 2005, pp. 760–767. doi:10.2514/1.3479.

[12] Egorov, I. V., Novikov, F. V., and Fedorov, A. V., "Numerical Modeling of the Disturbances of the Separated Flow in a Rounded Compression Corner," *Fluid Dynamics*, Vol. 41, No. 4, 2006, pp. 521–530. doi:10.1007/s10697-006-0070-7.

[13] Novikov, A., Egorov, I., and Fedorov, A., "Direct Numerical Simulation of Wave Packets in Hypersonic Compression-Corner Flow," *AIAA Journal*, Vol. 54, No. 7, 2016, pp. 2034–2050. doi:10.2514/1.J054665.

[14] Pandey, A., Casper, K. M., Spillers, R. W., Soehnel, M., and Spitzer, S., "Hypersonic Shock Wave-Boundary-Layer Interaction on the Control Surface of a Slender Cone," *AIAA SciTech 2020 Forum*, 2020, p. 0815. doi:10.2514/6.2020-0815.

[15] Benitez, E. K., Jewell, J. S., Schneider, S. P., and Esquieu, S., "Instability measurements on an axisymmetric separation bubble at Mach 6," *AIAA Aviation 2020 Forum*, 2020, pp. 1–29. doi:10.2514/6.2020-3072.

[16] McKiernan, G. R., and Schneider, S. P., "Instability and Transition on a Cone with a Slice and Ramp at Mach 6," *AIAA SciTech 2021 Forum*, 2021. doi:10.2514/6.2021-0249.

[17] Butler, C. S., and Laurence, S. J., "Interaction of second-mode disturbances with an incipiently separated compression-corner flow," *Journal of Fluid Mechanics*, Vol. 913, No. April, 2021, p. R4. doi:10.1017/jfm.2021.91.

[18] Leinemann, M., Radespiel, R., Munoz, F., Esquieu, S., McKiernan, G., and Schneider, S. P., "Boundary Layer Transition on a Generic Model of Control Flaps in Hypersonic Flow," *2019 AIAA SciTech Forum*, 2019. doi:10.2514/6.2019-1908.

[19] Pandey, A., Casper, K. M., Soehnel, M., Spillers, R. W., Bhakta, R., and Beresh, S. J., "Hypersonic Fluid-Structure Interaction on the Control Surface of a Slender Cone," *AIAA SciTech 2021*, 2021. doi::10.2514/6.2021-0909.

[20] Fujii, K., Hirabayashi, N., Koyama, T., Tsuda, S., Nakagawa, M., Itabashi, Y., and Nakamura, A., "A Measurement of Instability Wave in the Hypersonic Boundary-Layer on a Sharp Cone," *41st AIAA Fluid Dynamics Conference and Exhibit*, 2011, pp. AIAA Paper 2011–3871. doi::10.2514/6.2011-3871.

[21] Laurence, S. J., Wagner, A., and Hannemann, K., "Experimental study of second-mode instability growth and breakdown in a hypersonic boundary layer using high-speed schlieren visualization," *Journal of Fluid Mechanics*, Vol. 797, 2016, pp. 471–503. doi:10.1017/jfm.2016.280.

[22] Casper, K. M., Beresh, S. J., Henfling, J. F., Spillers, R. W., Pruett, B. O., and Schneider, S. P., "Hypersonic wind-tunnel measurements of boundary-layer transition on a slender cone," *AIAA Journal*, Vol. 54, No. 4, 2016, pp. 1250–1263. doi:10.2514/1.J054033.

[23] Craig, S. A., Humble, R. A., Hofferth, J. W., and Saric, W. S., "Nonlinear behaviour of the Mack mode in a hypersonic boundary layer," *Journal of Fluid Mechanics*, Vol. 872, 2019, pp. 74–99. doi:10.1017/jfm.2019.359.

[24] Parziale, N. J., Shepherd, J. E., and Hornung, H. G., "Observations of hypervelocity boundary-layer instability," *Journal of Fluid Mechanics*, Vol. 781, 2015, pp. 87–112. doi:10.1017/jfm.2015.489.

[25] Benitez, E. K., Jewell, J. S., and Schneider, S. P., "Focused Laser Differential Interferometry with Contoured Tunnel Windows," *AIAA Journal*, Vol. 59, No. 2, 2021, pp. 419–429. doi:10.2514/1.J060081.

[26] Xiong, Y., Yu, T., Lin, L., Zhao, J., and Wu, J., "Nonlinear Instability Characterization of Hypersonic Laminar Boundary Layer," *AIAA Journal*, Vol. 58, No. 12, 2020, pp. 5254–5263. doi:10.2514/1.J059263.

[27] Weisberger, J. M., Bathel, B. F., Herring, G. C., Buck, G. M., Jones, S. B., and Cavone, A. A., "Multi-point line focused laser differential interferometer for high-speed flow fluctuation measurements," *Applied Optics*, Vol. 59, No. 35, 2020, pp. 11180–11195. doi:10.1364/AO.411006.

[28] Gragston, M., Siddiqui, F., and Schmisseur, J. D., "Detection of second-mode instabilities on a flared cone in Mach 6 quiet flow with linear array focused laser differential interferometry," *Experiments in Fluids*, Vol. 62, No. 81, 2021. doi:10.1007/s00348-021-03188-6.

[29] Sadagopan, A., Huang, D., Jirasek, A., Seidel, J., Pandey, A., and Casper, K. M., "Joint Experimental/Computational Study of Fluid-Thermal-Structural Interaction of a Cone-Slice-Ramp in Hypersonic Flow," *AIAA SciTech 2022*, 2022.

[30] Schmidt, B. E., and Shepherd, J. E., "Analysis of focused laser differential interferometry," *Applied Optics*, Vol. 54, No. 28, 2015, pp. 8459–8472. doi:10.1364/AO.54.008459.

[31] Lawson, J. M., Neet, M. C., Grossman, I. J., and Austin, J. M., "Static and dynamic characterization of a focused laser diferential interferometer," *Experiments in Fluids*, Vol. 61, No. 187, 2020. doi:10.1007/s00348-020-03013-6.

[32] Towne, A., Schmidt, O. T., and Colonius, T., "Spectral proper orthogonal decomposition and its relationship to dynamic mode decomposition and resolvent analysis," *Journal of Fluid Mechanics*, Vol. 847, 2018, pp. 821–867. doi:10.1017/jfm.2018.283.

[33] Schmidt, O. T., and Towne, A., "An efficient streaming algorithm for spectral proper orthogonal decomposition," *Computer Physics Communications*, Vol. 237, No. 4, 2019, pp. 98–109. doi:10.1016/j.cpc.2018.11.009.